

# *Euclid*: Constraining dark energy coupled to electromagnetism using astrophysical and laboratory data<sup>★</sup>

M. Martinelli<sup>1</sup>, C. J. A. P. Martins<sup>2,3</sup>, S. Nesseris<sup>1</sup>, I. Tutusaus<sup>4,5,6</sup>, A. Blanchard<sup>5</sup>, S. Camera<sup>7,8,9</sup>, C. Carbone<sup>10</sup>, S. Casas<sup>11</sup>, V. Pettorino<sup>11</sup>, Z. Sakr<sup>5,12</sup>, V. Yankelevich<sup>13</sup>, D. Sapone<sup>14</sup>, A. Amara<sup>15</sup>, N. Auricchio<sup>16</sup>, C. Bodendorf<sup>17</sup>, D. Bonino<sup>9</sup>, E. Branchini<sup>18,19</sup>, V. Capobianco<sup>9</sup>, J. Carretero<sup>20</sup>, M. Castellano<sup>21</sup>, S. Cavuoti<sup>22,23,24</sup>, A. Cimatti<sup>25,26</sup>, R. Cledassou<sup>27,28</sup>, L. Corcione<sup>9</sup>, A. Costille<sup>29</sup>, H. Degaudenzi<sup>30</sup>, M. Douspis<sup>31</sup>, F. Dubath<sup>30</sup>, S. Dusini<sup>32</sup>, A. Ealet<sup>33</sup>, S. Ferriol<sup>33</sup>, M. Frailis<sup>34</sup>, E. Franceschi<sup>16</sup>, B. Garilli<sup>10</sup>, C. Giocoli<sup>35,36</sup>, A. Grazian<sup>37</sup>, F. Grupp<sup>17,38</sup>, S. V. H. Haugan<sup>39</sup>, W. Holmes<sup>40</sup>, F. Hormuth<sup>41,42</sup>, K. Jahnke<sup>42</sup>, A. Kiessling<sup>40</sup>, M. Kümmel<sup>38</sup>, M. Kunz<sup>43</sup>, H. Kurki-Suonio<sup>44</sup>, S. Ligi<sup>9</sup>, P. B. Lilje<sup>39</sup>, I. Lloro<sup>45</sup>, O. Mansutti<sup>34</sup>, O. Marggraf<sup>46</sup>, K. Markovic<sup>40</sup>, R. Massey<sup>47</sup>, M. Meneghetti<sup>16,48</sup>, G. Meylan<sup>49</sup>, L. Moscardini<sup>16,25,50</sup>, S. M. Niemi<sup>51</sup>, C. Padilla<sup>20</sup>, S. Paltani<sup>30</sup>, F. Pasian<sup>34</sup>, K. Pedersen<sup>52</sup>, S. Pires<sup>11</sup>, M. Poncet<sup>28</sup>, L. Popa<sup>53</sup>, F. Raison<sup>17</sup>, R. Rebolo<sup>54,55</sup>, J. Rhodes<sup>40</sup>, M. Roncarelli<sup>16,25</sup>, E. Rossetti<sup>25</sup>, R. Saglia<sup>17,38</sup>, A. Secroun<sup>56</sup>, G. Seidel<sup>42</sup>, S. Serrano<sup>4,6</sup>, C. Sirignano<sup>32,57</sup>, G. Sirri<sup>50</sup>, J.-L. Starck<sup>11</sup>, D. Tavagnacco<sup>34</sup>, A. N. Taylor<sup>58</sup>, I. Tereno<sup>59,60</sup>, R. Toledo-Moreo<sup>61</sup>, L. Valenziano<sup>16,50</sup>, Y. Wang<sup>62</sup>, G. Zamorani<sup>16</sup>, J. Zoubian<sup>56</sup>, M. Baldi<sup>16,50,63</sup>, M. Brescia<sup>24</sup>, G. Congedo<sup>58</sup>, L. Conversi<sup>64,65</sup>, Y. Copin<sup>33</sup>, G. Fabbian<sup>66</sup>, R. Farinelli<sup>67</sup>, E. Medinaceli<sup>16</sup>, S. Mei<sup>68</sup>, G. Polenta<sup>69</sup>, E. Romelli<sup>34</sup>, and T. Vassallo<sup>38</sup>

(Affiliations can be found after the references)

Received 20 May 2021 / Accepted 19 August 2021

## ABSTRACT

In physically realistic, scalar-field-based dynamical dark energy models (including, e.g., quintessence), one naturally expects the scalar field to couple to the rest of the model's degrees of freedom. In particular, a coupling to the electromagnetic sector leads to a time (redshift) dependence in the fine-structure constant and a violation of the weak equivalence principle. Here we extend the previous *Euclid* forecast constraints on dark energy models to this enlarged (but physically more realistic) parameter space, and forecast how well *Euclid*, together with high-resolution spectroscopic data and local experiments, can constrain these models. Our analysis combines simulated *Euclid* data products with astrophysical measurements of the fine-structure constant,  $\alpha$ , and local experimental constraints, and it includes both parametric and non-parametric methods. For the astrophysical measurements of  $\alpha$ , we consider both the currently available data and a simulated dataset representative of Extremely Large Telescope measurements that are expected to be available in the 2030s. Our parametric analysis shows that in the latter case, the inclusion of astrophysical and local data improves the *Euclid* dark energy figure of merit by between 8% and 26%, depending on the correct fiducial model, with the improvements being larger in the null case where the fiducial coupling to the electromagnetic sector is vanishing. These improvements would be smaller with the current astrophysical data. Moreover, we illustrate how a genetic algorithms based reconstruction provides a null test for the presence of the coupling. Our results highlight the importance of complementing surveys like *Euclid* with external data products, in order to accurately test the wider parameter spaces of physically motivated paradigms.

**Key words.** cosmology: observations – cosmological parameters – space vehicles: instruments – methods: data analysis – methods: statistical – surveys

## 1. Introduction

The search for the physical mechanism underlying the observed low-redshift acceleration of the Universe is a pressing objective of contemporary cosmology. A first task in this endeavour is to map the behaviour of the energy density (or its equation of state parameter) of the dark energy component as a function of redshift – with the simplest case of a cosmological constant corresponding to a constant energy density. To this end, simple parametrizations are often used, commensurate with the limited constraining power of the currently available data, for instance for the dark energy equation of state parameter one has a tight constraint on its present value and a reasonable constraint on its rate of change. Even so, these parametrizations should be seen as convenient proxies for more physically realistic models, possi-

bly containing a larger number of model parameters. While such wider parameter spaces are not significantly constrained by current data, they can in principle be constrained by future surveys.

*Euclid* is a medium-class mission of the European Space Agency due for launch in 2022. Using a visible imager (Cropper et al. 2018) and a near-infrared spectrophotometric instrument (Costille et al. 2018), it will perform a photometric and spectroscopic galaxy survey over 15 000 squared degrees of extra-galactic sky, plus a deeper survey over 40 squared degrees (Laureijs et al. 2011). The main goal of *Euclid* is to provide measurements of the geometry of the Universe and the growth of structures up to redshift  $z \sim 2$ , and beyond. *Euclid* will provide three primary cosmological probes: weak gravitational lensing, the clustering of galaxies using measurements from the photometric galaxy survey, and the clustering of galaxies of the spectroscopic survey. The latter will enable precise measurements of the baryon acoustic oscillations and

<sup>★</sup> This paper is published on behalf of the Euclid Consortium.

redshift-space distortions. Given the high complementarity of these large-scale structure probes, we expect very precise constraints from *Euclid* observations, not only on the concordance cosmological constant and cold dark matter ( $\Lambda$ CDM) model, but also on theoretical extensions of it (see e.g., [Euclid Collaboration 2020](#); [Tutusaus et al. 2020](#)).

In [Euclid Collaboration \(2020\)](#); hereafter EC20), the constraining power of *Euclid* on dark energy models was estimated using the common Chevallier-Polarski-Linder (CPL) parameterization ([Chevallier & Polarski 2001](#); [Linder 2003](#)) as a phenomenological proxy for generic dynamical dark energy models. However, in physically realistic, scalar-field-based dynamical dark energy models (including, e.g. quintessence), one naturally expects the scalar field to couple to other sectors of the theory, unless unknown symmetries suppress such a coupling. Here we focus on the possible coupling of a dark energy scalar field to the electromagnetic sector, which would lead to a time (redshift) dependence of the fine-structure constant,  $\alpha$ , a violation of the Einstein equivalence principle ([Carroll 1998](#); [Dvali & Zaldarriaga 2002](#); [Chiba & Kohri 2002](#)), and also a violation of the distance duality relation. Forecast constraints on the latter from *Euclid* and contemporary surveys are discussed in [Martinelli et al. \(2020\)](#).

There are two immediate consequences of this. The first is that one should deal with a wider parameter space: the coupling of the scalar field to the electromagnetic sector is a further relevant parameter, all the more so because, as can be seen in what follows, it is degenerate with the parameters describing the dark energy evolution. The second consequence is that *Euclid*, at least with its primary probes, is not able to constrain such a coupling, as its observables are not sensitive to the variation in the fine-structure constant, and therefore one needs to add astrophysical and local constraints on  $\alpha$  and the Einstein equivalence principle to the analysis in order to test this kind of scenario. A recent review of the synergies between these astrophysical and local tests and cosmological observations is given in [Martins \(2017\)](#).

Therefore our analysis in this work, which builds upon previous works by [Calabrese et al. \(2014\)](#), [Martins et al. \(2016\)](#), and [EC20](#), has two main goals: firstly, to forecast how well *Euclid* (in combination with external data, specifically high-resolution spectroscopic data and local experimental results) can constrain these models, and secondly, to quantify the change in forecast constraints on CPL parameters when the assumption of a vanishing coupling between the dark energy driving scalar field and electromagnetism is removed.

The plan of the rest of the paper is as follows. In Sect. 2 we review theoretical models relating dynamical dark energy and a varying fine-structure constant. In Sect. 3 we describe the currently available data and the forecast future data used in this work, including both *Euclid* measurements and astrophysical and local data. In Sects. 4 and 5 we describe the analysis methods used in this study: a standard likelihood analysis for the CPL parametrization and a model-independent reconstruction using genetic algorithms. We present the results obtained with a likelihood analysis in Sect. 6 and the results derived with the genetic algorithms in Sect. 7. We present our discussion and conclusions in Sect. 8.

## 2. Dynamical dark energy and varying alpha

Dynamical scalar fields in an effective four-dimensional field theory are naturally expected to couple to the rest of the theory, unless a still unknown symmetry is postulated to suppress these couplings. In particular, these couplings unavoidably

exist in string theory ([Taylor & Veneziano 1988](#); [Casas et al. 1991, 1992](#)), and their cosmological role is especially interesting in models where such a dilaton-type scalar field is also responsible for the acceleration of the universe ([Carroll 1998](#); [Dvali & Zaldarriaga 2002](#); [Chiba & Kohri 2002](#); [Damour et al. 2002](#)). In what follows, we assume this coupling does exist for the dynamical degree of freedom responsible for the dark energy. Specifically we are interested in the coupling between a canonical scalar field, denoted  $\phi$ , and the electromagnetic sector, which stems from a gauge kinetic function  $B_F(\phi)$

$$\mathcal{L}_{\phi F} = -\frac{1}{4}B_F(\phi)F_{\mu\nu}F^{\mu\nu}. \quad (1)$$

Since the local behaviour of electromagnetism is extremely well known and any variation in  $\alpha$  is constrained to be very small (as further discussed below), one can safely assume this function to be linear,

$$B_F(\phi) = 1 - \zeta\kappa(\phi - \phi_0), \quad (2)$$

(where we have defined  $\kappa^2 = 8\pi G$ ) since, as has been pointed out in [Dvali & Zaldarriaga \(2002\)](#), the absence of such a term would require the presence of a  $\phi \rightarrow -\phi$  symmetry. Such a symmetry must be broken throughout most of the cosmological evolution, because  $\phi$  is a time-dependent field, changing (possibly very slowly) as the universe expands. In other words, the absence of such a term would require fine-tuning. With this definition  $\zeta$  is a dimensionless coupling, which will be crucial in our subsequent discussion. As is physically clear, the relevant parameter in the cosmological evolution is the field displacement relative to its present-day value (in particular  $\phi_0$  could be freely set to zero).

With these assumptions one can explicitly relate the evolution of  $\alpha$  to that of dark energy, as in [Calabrese et al. \(2011\)](#), whose derivation we summarize. The evolution of  $\alpha$  can be written as

$$\frac{\Delta\alpha}{\alpha} \equiv \frac{\alpha - \alpha_0}{\alpha_0} = B_F^{-1}(\phi) - 1 = \zeta\kappa(\phi - \phi_0). \quad (3)$$

Defining the fraction of the dark energy density as

$$\Omega_\phi(z) \equiv \frac{\rho_\phi(z)}{\rho_{\text{tot}}(z)} \simeq \frac{\rho_\phi(z)}{\rho_\phi(z) + \rho_m(z)}, \quad (4)$$

where in the last step we have neglected the contribution from radiation (since we are interested in low redshifts,  $z < 5$ , where it is indeed negligible), the evolution of the putative scalar field can be expressed in terms of the dark energy properties  $\Omega_\phi$  and  $w_\phi$  as ([Nunes & Lidsey 2004](#))

$$1 + w_\phi = \frac{(\kappa\phi')^2}{3\Omega_\phi}, \quad (5)$$

with the prime denoting the derivative with respect to the logarithm of the scale factor. We finally obtain

$$\frac{\Delta\alpha}{\alpha}(z) = \zeta \int_0^z \sqrt{3\Omega_\phi(z') [1 + w_\phi(z')]} \frac{dz'}{1 + z'}. \quad (6)$$

The above relation assumes a canonical scalar field, but the argument can be repeated for phantom fields, as discussed in [Vielzeuf & Martins \(2014\)](#), leading to

$$\frac{\Delta\alpha}{\alpha}(z) = -\zeta \int_0^z \sqrt{3\Omega_\phi(z') |1 + w_\phi(z')|} \frac{dz'}{1 + z'}. \quad (7)$$

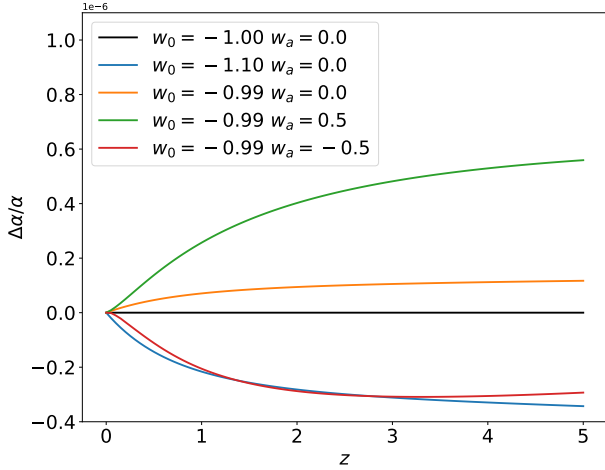


**Fig. 1.** Example trends in redshift for the variation in  $\alpha$  changing the CPL parameters. The values of the other cosmological parameters entering Eqs. (6) and (7) are  $\Omega_m = 0.32$ , and  $\zeta = 10^{-6}$ .

Physically, the change of sign stems from the fact that one expects phantom fields to roll up the potential rather than down. Naturally, the two definitions match across the phantom divide ( $w = -1$ ). These relations have been applied to several possible choices for the scalar field equation of state (Martins 2017). Here we choose to parameterize the  $w_\phi$  function following the CPL parameterization (Chevallier & Polarski 2001; Linder 2003). In this case the dark energy equation of state has the form

$$w_{\text{CPL}}(z) = w_0 + w_a \frac{z}{1+z}, \quad (8)$$

while the fraction of energy density provided by the scalar field is easily found to be

$$\Omega_{\text{CPL}}(z) = \frac{1 - \Omega_m}{1 - \Omega_m + \Omega_m (1+z)^{-3(w_0+w_a)} e^{3w_a z/(1+z)}}, \quad (9)$$

where we assumed a flat Universe, with a vanishing curvature parameter  $\Omega_K = 0$ . When going beyond background probes, the CPL parameterization is commonly combined with the Parametrized Post-Friedmann (PPF) framework for DE perturbations (Hu & Sawicki 2007; Hu 2008; Fang et al. 2008). The dependence of Eqs. (6) and (7) on  $w_\phi(z)$  also makes it clear that we should expect (as discussed in Calabrese et al. 2014) degeneracies between the coupling  $\zeta$  and the CPL dark energy parameters,  $w_0$  and  $w_a$ , while the correlation with the matter density should be much weaker. On the other hand, note that the  $\alpha$  variation is independent of the Hubble constant. In Fig. 1 we show the theoretical prediction for the redshift trend of  $\Delta\alpha/\alpha$  for several values of the CPL parameters  $w_0$  and  $w_a$ . It can be seen how we also expect degeneracies between these parameters, with constant  $w(z)$  cases ( $w_a = 0$ ) that produce redshift evolution very similar to cases where  $w_a \neq 0$ .

A varying  $\alpha$  violates the Einstein equivalence principle since it clearly violates local position invariance. The realization that varying fundamental couplings also induce violations of the universality of free fall goes back at least to the work of Dicke (Dicke 1964) – we refer the reader to Damour & Donoghue (2010) for a recent thorough discussion. The key point in our present context is that a light scalar field, such as the one we are considering here, inevitably couples to nucleons due to the  $\alpha$  dependence of their masses, and therefore it mediates an isotope-dependent long-range force. This can be simply quantified through the dimensionless Eötvös parameter  $\eta$ , which

describes the level of violation of the Weak Equivalence Principle (WEP). One can show that for the class of models we are considering here, the Eötvös parameter and the dimensionless coupling  $\zeta$  are simply related by (Dvali & Zaldarriaga 2002; Chiba & Kohri 2002; Damour & Donoghue 2010)

$$\eta \approx 10^{-3} \zeta^2; \quad (10)$$

therefore local experimental constraints on the former can be used to constrain the latter.

We note that there is in principle an additional source term driving the evolution of the scalar field, due to a  $F^2 B'_F$  term. By comparison to the standard (kinetic and potential energy) terms, the contribution of this term is subdominant, both because its average is zero for a radiation fluid and because the corresponding term for the baryonic density is constrained for the reasons discussed in the previous paragraph. For these reasons, in what follows we neglect this term, which would lead to spatial and environmental dependencies. We nevertheless note that this term can play a role in cosmological scenarios where the dominant standard term is suppressed, such as the models studied in Olive & Pospelov (2008), Silva et al. (2014), Pinho et al. (2017).

Finally, another important observable is the current drift rate of the value of  $\alpha$ , which can easily be found to be

$$D \equiv \left( \frac{\dot{\alpha}}{\alpha} \right)_0 = \mp \zeta H_0 \sqrt{3\Omega_{\phi 0} |1 + w_0|}, \quad (11)$$

with the minus and plus signs corresponding respectively to the canonical and phantom cases. Naturally, the drift rate depends on the present value of the dark energy equation of state (and vanishes for  $w_0 = -1$ ), but it is independent of  $w_a$ . This observable provides a second way to constrain these models using local experiments, since the drift rate can be constrained using laboratory experiments which compare atomic clocks based on transitions with different sensitivities to  $\alpha$ .

### 3. Available and future data

The purpose of this work is to constrain canonical scalar-field based dynamical dark energy models which allow for the possible variation in the fine-structure constant, as detailed in Sect. 2, using both currently available data and the ones expected from future surveys. In particular, we use data from observations of quasi-stellar object (QSO) spectral lines from archival datasets and dedicated measurements, complemented by laboratory constraints, detailed in Sect. 3.1, as well as forecast data for the future measurements of  $\Delta\alpha/\alpha$  from the Extremely Large Telescope (ELT) as discussed in Leite et al. (2016); the assumptions made to generate mock datasets for this experiment are shown in Sect. 3.2.

However, as pointed out in Calabrese et al. (2014) and as can also be seen in Eqs. (6) and (7), the coupling parameter that drives the variation in  $\alpha$  is significantly degenerate with other standard cosmological parameters, namely  $\Omega_m$ ,  $w_0$  and  $w_a$ . The constraining power of *Euclid* on these parameters is therefore crucial if one wants to constrain this kind of models.

#### 3.1. Currently available data for $\alpha$ variation

Our astrophysical data consists of high-resolution spectroscopy tests of the stability of  $\alpha$ . These measurements are done in low-density absorption clouds along the line of sight of bright quasars, typically with wavelength resolution  $R = \lambda/\Delta\lambda \sim$

50 000 (although the exact value is different for different measurements). We use a total of 319 measurements, of which 293 come from the analysis of archival data by Webb et al. (2011) and the remaining 26 are more recent dedicated measurements (Martins 2017; Murphy & Cooksey 2017; Welsh et al. 2020; Milaković et al. 2021). The latter subset is therefore smaller than the former, but it contains more stringent measurements, so overall the archival and dedicated subsets have comparable constraining power (Martins & Vila Miñana 2019). Overall, this dataset includes measurements up to redshift  $z \sim 4.18$ .

In our analysis we assume a homogeneous and isotropic universe, and therefore we also assume that the measurements of  $\alpha$  depend only on redshift. That said, we note that Webb et al. (2011) has claimed a spatial variation in  $\alpha$ , consistent with a dipole-like behaviour and with an amplitude at the parts per million level of relative variation, although this claim has been disputed by Whitmore & Murphy (2015). If these claims prove to be correct, the main implication would be ruling out the assumption of a Friedmann-Lemaître-Robertson-Walker universe. Such a scenario would therefore require a separate analysis.

Additionally, the current drift rate of  $\alpha$  is constrained by local comparison experiments between atomic clocks, with the most stringent bound being the one by Lange et al. (2021)

$$D|_{\text{obs}} \equiv \left( \frac{\dot{\alpha}}{\alpha} \right)_0 = (1.0 \pm 1.1) \times 10^{-18} \text{ yr}^{-1}. \quad (12)$$

Last but not least, we also use the recent MICROSCOPE bound on the Eötvös parameter of Touboul et al. (2019)

$$\eta = (-0.1 \pm 1.3) \times 10^{-14}, \quad (13)$$

which, as previously discussed, constrains the model's coupling to the electromagnetic sector.

In the rest of the paper, we refer to the combination of all these data as current  $\alpha$  data, and we show the constraints produced by such a combination. However, we note that the 293 archival data and the 26 dedicated ones are in slight tension with each other (Martins 2017; Martins & Vila Miñana 2019). Despite assuming here that they can be safely combined, we discuss this issue in more detail in Appendix A.

In our analysis, we do not include geophysical constraints on the variation in  $\alpha$ , coming from the Oklo natural nuclear reactor (Fujii et al. 2002; Davis & Hamdan 2015) and meteoric data (Olive et al. 2004). This is motivated by the model dependence of such data, as they only provide stringent constraints on  $\alpha$  if one assumes that only the fine-structure constant can vary while the strong sector of the theory is unchanged, which is a simplistic assumption for constraints that stem from nuclear-physics processes (Martins 2017). Thus, they are less reliable than the spectroscopic and atomic clock data.

### 3.2. ELT forecast

Here we assume a future dataset to be put together by the high-resolution ultra-stable spectrograph currently known as HIRES (Marconi et al. 2020), that will operate the 39.3 m Extremely Large Telescope. For simplicity, we assume a set of 50  $\alpha$  measurements, uniformly spaced in the redshift range  $0.7 \leq z \leq 3.2$ , each with an uncertainty of 0.03 parts per million, which is commensurate with the assumptions in Leite et al. (2016) and the Top-Level Requirements for the instrument (Liske et al. 2014).

With these specifications in hand, we generated the fiducial redshift dependence of  $\Delta\alpha/\alpha$  using Eqs. (6) and (7) with two different fiducial cosmologies, dubbed  $\Lambda$ CDM and  $\zeta w_0 w_a$ CDM,

**Table 1.** Fiducial values for the two cosmologies considered here and used to obtain the mock datasets for ELT measurements.

Parameter symbol	$\Lambda$ CDM	$\zeta w_0 w_a$ CDM
$\Omega_m$	0.32	0.32
$h$	0.67	0.67
$w_0$	-1.	-0.94
$w_a$	0	0.1
$\zeta$	0	$-5 \times 10^{-8}$

**Notes.** Here  $h$  is the reduced Hubble parameter, corresponding to  $H_0/(100 \text{ km s}^{-1} \text{ Mpc}^{-1})$ .

shown in Table 1. These two fiducial cosmologies correspond to a standard case in which no  $\alpha$  variation is present ( $\Lambda$ CDM) and to one where instead we assume the coupling parameter  $\zeta$  is non vanishing, but still compatible with the laboratory constraints discussed in Sect. 3.1, and a dark energy component that does not behave as a cosmological constant. In this second case ( $\zeta w_0 w_a$ CDM) the value of  $\alpha$  varies in redshift and we aim at finding signatures of such variation.

Once the fiducial behaviour for  $\Delta\alpha/\alpha$  is obtained as discussed earlier, we then create the corresponding mock dataset drawing the data points at each redshift from a Gaussian distribution centred at the fiducial model and with  $\sigma$  the expected observational error of HIRES. We assume such errors to be uncorrelated, which observationally is a safe assumption since each measurement comes from a high-resolution ( $R \sim 100\,000$ ) signal-to-noise limited spectrum of a point source along a different line of sight.

### 3.3. Euclid forecast methodology and Fisher matrices

As previously discussed, observations from Large Scale Structures probe are not very sensitive to variations in  $\alpha$  and therefore they cannot significantly constrain the coupling  $\zeta$ . They are however crucial to break the degeneracies between the coupling and the cosmological parameters, and can be therefore combined with the datasets discussed above. In this work we consider specifically *Euclid* as our probe of LSS. It is worth mentioning that, strictly speaking, LSS probes can provide some relevant constraints on variations in  $\alpha$ . In Albareti et al. (2015), for example, constraints on  $\Delta\alpha/\alpha$  were provided using the OIII doublet from BOSS DR12 quasar spectra. Following similar approaches, we could extract information on the variation in  $\alpha$  from the future *Euclid* data. Furthermore, a type-Ia supernovae survey using *Euclid* data (Astier et al. 2014) could provide some information on the variation in  $\alpha$ , as illustrated in Calabrese et al. (2014). However, we prefer to focus here on the main *Euclid* probes and their constraints on the cosmological parameters.

In this work, in order to forecast the constraints from the future *Euclid* data, we follow the methodology presented in EC20. We consider a Fisher matrix formalism and make use of the TotallySAF<sup>1</sup> code (Yahia-Cherif et al. 2021; Tutusaus et al. 2020) validated therein for the main *Euclid* probes: spectroscopic galaxy clustering (GCsp), photometric galaxy clustering (GCph), weak lensing (WL), and the cross-correlation (XC) terms between the photometric probes. As was done in EC20, we neglect any correlation between the spectroscopic and photometric probes.

<sup>1</sup> [https://github.com/syahiacherif/TotallySAF\\_Alpha](https://github.com/syahiacherif/TotallySAF_Alpha)

Starting with the spectroscopic probe, we build a Fisher matrix for the observed anisotropic power spectrum of H- $\alpha$  emitters (see Eq. (87) in EC20), accounting for a phenomenological model for non-linearities, the Alcock-Paczynski effect, redshift-space distortions, and the Fingers-of-God effect. As in EC20, we consider two scenarios for these forecasts. In the optimistic case, we consider all scales up to a maximum of  $k_{\max} = 0.30 h \text{ Mpc}^{-1}$ , and we fix the nuisance parameters associated to non-linearities. In the pessimistic scenario we limit our analysis to scales  $k < k_{\max} = 0.25 h \text{ Mpc}^{-1}$  and marginalize over the non-linear nuisance parameters.

With respect to the photometric probes, we build a Fisher matrix for the tomographically binned projected angular power spectra. The same formalism is used for WL, GCph, and their XC terms, with the only difference being the kernels used in the projection from the power spectrum of matter perturbations to the spherical-harmonic space observable. As in EC20, we use the Limber, flat-sky and spatially flat approximations (Kitching et al. 2017; Kilbinger et al. 2017; Taylor et al. 2018). We also neglect redshift-space distortions, magnification, and other relativistic effects (Deshpande et al. 2020), but marginalize over the galaxy bias and intrinsic alignment nuisance parameters. We refer to EC20 for all the details on the modelling. As in the spectroscopic case, we consider two different scenarios in our forecasts. In the optimistic setting, we consider all multipoles between  $\ell_{\min} = 10$  and  $\ell_{\max} = 3000$  for GCph and the XC terms and  $\ell_{\max} = 5000$  for WL. We then combine with the spectroscopic constraints assuming they are independent. In the pessimistic scenario, we limit the multipoles to  $\ell_{\max} = 750$  for GCph and the XC terms and  $\ell_{\max} = 1500$  for WL. In this case, when combining with the spectroscopic probe, we introduce a redshift cut of  $z < 0.9$  for GCph and the XC terms, in order to remove any possible correlation with the spectroscopic sample starting at  $z = 0.9$ .

In accordance with Sect. 2 and EC20, we consider in this work a cosmological model with a dark energy equation of state parametrized with the CPL parametrization and with  $\Omega_K = 0$ . In contrast with EC20, here we do not consider just a single  $\Lambda$ CDM fiducial (since under the assumptions of the present work there would be no  $\alpha$  variation in that case), and obtain the Fisher matrices in both assumed cosmologies of Table 1. In addition to these assumed parameters, the analysis of EC20 also requires to specify the fiducial values of other cosmological parameters, namely the baryon energy density ( $\Omega_b = 0.05$ ), the primordial spectral index ( $n_s = 0.96$ ) and the current amplitude of density perturbations ( $\sigma_8 = 0.816$ ). These additional parameters take the same fiducial values in both the  $\Lambda$ CDM and  $\zeta w_0 w_a$ CDM cosmologies.

For completeness, and in order to compare with the results of this work, we provide in Table 2 the baseline *Euclid* forecasts obtained in EC20 for the relevant parameters in our analysis. We also note that the current constraints on the dark energy equation of state parameters are  $w_0 = -0.957 \pm 0.080$  and  $w_a = -0.29^{+0.32}_{-0.26}$ , using the combination of *Planck* 2018 temperature, polarization, and lensing measurements, together with type-Ia supernovae and baryon acoustic oscillations observations (Planck Collaboration VI 2020).

#### 4. Likelihood analysis for the CPL parametrization

Following the prescription for a possible  $\alpha$  variation described in Sect. 2, we want to combine current and forecast  $\alpha$  measurements with the information that will be brought by *Euclid*, thus investigating how this survey will improve our constraints on this possible deviation from the standard cosmological paradigm.

**Table 2.** Baseline *Euclid* forecast uncertainties for the relevant parameters in this work,  $\Omega_m$ ,  $h$ ,  $w_0$ , and  $w_a$ , obtained in EC20.

Parameter symbol	Pessimistic	Optimistic
$\sigma(\Omega_m)$	0.0038	0.0018
$\sigma(h)$	0.0037	0.0010
$\sigma(w_0)$	0.040	0.025
$\sigma(w_a)$	0.17	0.092

While in Sect. 3.3 we discussed how *Euclid* constraints can be predicted using the Fisher matrix approach, the strong non-Gaussian nature of the joint cosmology and fundamental physics parameter space in varying  $\alpha$  models (Calabrese et al. 2014) makes this approach unfeasible for both the current and future measurements that we are interested in.

Therefore, we rely here on an MCMC approach, using the publicly available sampler Cobaya (Torrado & Lewis 2021), which exploits a Metropolis-Hastings (MH) algorithm (Lewis & Bridle 2002; Lewis 2013). We sample the matter density parameter  $\Omega_m$ , the Hubble constant  $H_0$ , the two parameters of the CPL parameterization  $w_0$  and  $w_a$ , and the coupling parameter  $\zeta$  that connects the dynamical dark energy scalar field to the electromagnetic sector (see Sect. 2). The posterior distribution  $P(\theta)$  that we reconstruct with this method at each point  $\theta = (\Omega_m, H_0, w_0, w_a, \zeta)$  of the parameter space contains information coming from both  $\alpha$  measurements and the *Euclid* survey,

$$P(\theta) \propto \mathcal{L}_\alpha(\theta) \mathcal{L}_{Euclid}(\theta), \quad (14)$$

where  $\mathcal{L}_\alpha$  and  $\mathcal{L}_{Euclid}$  are the likelihoods of the  $\alpha$  and *Euclid* datasets respectively, and we assumed that the two probes are uncorrelated.

The *Euclid* likelihood is constructed using the Fisher matrix  $F$  described in Sect. 3.3, and it simply exploits the Gaussian assumption done to obtain these:

$$-\ln \mathcal{L}_{Euclid} \propto \frac{1}{2} (\theta - \theta_{\text{fid}})^T \tilde{F} (\theta - \theta_{\text{fid}}), \quad (15)$$

where  $\tilde{F}$  is the Fisher matrix  $F$  marginalized over all parameters that are not contained in our sampled parameter space, while  $\theta_{\text{fid}}$  is the fiducial cosmology under examination, which can be one of the two shown in Table 1.

On the other hand, the  $\alpha$  likelihood contains two different contributions, again assumed to be uncorrelated, with

$$-\ln \mathcal{L}_\alpha \propto -(\ln \mathcal{L}_{\text{QSO}} + \ln \mathcal{L}_{\text{clocks}}), \quad (16)$$

with the first contribution given by observations of quasar absorption systems and the second, coming from atomic clocks measurements, giving a constraint on the possible coupling  $\zeta$  at present time. These two likelihoods are taken to be

$$-\ln \mathcal{L}_{\text{QSO}} \propto \frac{1}{2} \sum_i \frac{1}{\sigma_i^2} \left[ \frac{\Delta\alpha}{\alpha} \Big|_{\text{th}}(z_i) - \frac{\Delta\alpha}{\alpha} \Big|_{\text{obs}}(z_i) \right]^2, \quad (17)$$

and

$$-\ln \mathcal{L}_{\text{clocks}} \propto \frac{1}{2} \frac{(D|_{\text{th}} - D|_{\text{obs}})^2}{\sigma_D^2}, \quad (18)$$

where the th subscript indicates the theoretical predictions, given by Eqs. (6) and (7) for  $\Delta\alpha/\alpha$  and Eq. (11) for  $D$ , while the quantities labelled with the obs subscript and the corresponding errors are the measurements described in Sect. 3.

We therefore sample the parameter space described above and reconstruct the posterior of Eq. (14), using flat priors on all parameters except for the coupling  $\zeta$ , for which a Gaussian prior centred in  $\zeta = 0$  and with variance  $1.3 \times 10^{-14}$  is used. Such prior information is derived from the MICROSCOPE experiment discussed in Sect. 3.1, which directly constrains the Eötvös parameter  $\eta$ , which is related to the coupling  $\zeta$  via Eq. (10).

In addition, we obtain as derived parameters also the value of  $\Delta\alpha/\alpha$  in a set of equally spaced redshifts  $z_i$ . Obtaining the marginalized mean values of these derived parameters and their 68% confidence limit, we reconstruct the trend of the variation in  $\alpha$  with redshift in Sect. 6.

## 5. Genetic algorithm analysis

In our analysis we also use a non-parametric machine learning class of stochastic optimization methods, known as genetic algorithms (GA). These emulate natural selection, by using the data as proxies for the evolutionary pressure that drives the selection of the best-fitting functions in each generation. They are characterized by the notion of grammatical evolution, as described by the genetic operations of mutation and crossover. Specifically, a set of functions will evolve over time under the pressure of the data and the influence of the stochastic operators of crossover, that is the combination of different functions to form more complicated forms (offspring) that may fit the data better, and mutation, namely a random change in an individual function.

The GA have been used extensively to test for extensions of the standard model (Akrami et al. 2010), deviations from the cosmological constant model, both at the background and the perturbations level (Nesseris & Garcia-Bellido 2012; Arjona & Nesseris 2020a,b), to reconstruct a plethora of cosmological data, such as type Ia supernovae or CMB (Bogdanos & Nesseris (2009), Arjona (2020) or to reconstruct various null tests such as the so called Om statistic or the curvature test (Nesseris & Shafieloo 2010; Nesseris & Garcia-Bellido 2013a; Sapone et al. 2014).

In our analysis we fit the fine-structure data with the GA, however we solely focus on the coupling  $\zeta$ . From Eq. (3) it is clear that  $\zeta$  should be a constant within the context of the non-minimal coupling to the Maxwell field and the linear approximation of the gauge kinetic function  $B_F(\phi)$ , so we use the GA to test whether this assumption is actually supported by the data. In other words, we treat the constant  $\zeta$  case as a null test and use the GA to test for deviations from that behaviour. This approach has the advantage that the coupling  $\zeta$  is directly related to measurable quantities, especially in the case of the local experiments, see for example Eq. (10).

In detail, the analysis of the data with the GA proceeds as follows. First, we assume that the probability that a given function in the population will produce offspring, or equivalently its ‘productive success’, is proportional to its fitness. We quantify this fitness via a  $\chi^2$  statistic, which is obtained following the same likelihood computation used in Sect. 4. Second, an initial random group of functions is chosen, each representing an initial guess for the coupling, though they are allowed to be redshift dependent, that is  $\zeta = \zeta(z)$ .

We note that as the  $\alpha$  data extends to high redshifts, we base our GA grammar not in terms of the redshift  $z$ , but instead in terms of  $1 - a = \frac{z}{1+z}$ , something which is commonly used in other model independent methods as well, see for example Cattoen & Visser (2007), Lazkoz et al. (2013), Guimaraes & Lima (2011). This allows us to avoid any spurious reconstructions due to lack of convergence at high redshifts.

Then, in the case of the current data,  $\Delta\alpha/\alpha$  can be related directly to  $\zeta$  and compared to the data using Eqs. (6) and (7), for which we need to estimate the integral in the right hand side which can be done with the information provided by *Euclid*. We note that this integral is by default zero when the fiducial model is exactly the cosmological constant  $\Lambda$ CDM model, which means that the best-fit  $\zeta$  will remain indeterminate, so in our analysis we only use the *Euclid*  $\zeta_{w_0w_a}$ CDM fiducial model, as given in in Table 1. We then use 300 realizations and we calculate both the mean and variance of the integral, with the latter then included, via error propagation, in the error estimate of all reconstructed quantities. For the atomic clocks and the MICROSCOPE bound we use Eqs. (10) and (11) and the *Euclid*  $\zeta_{w_0w_a}$ CDM fiducial in a similar fashion.

After this is done, we can compare the predictions of the GA with the data and the fitness of every test function in the population can be calculated via a standard  $\chi^2$  statistic. Subsequently, the crossover and mutation operators are applied to a subset, usually the  $\sim 30\%$  best-fitting functions in every generation. These are chosen with the tournament selection – see Bogdanos & Nesseris (2009) for more details. We repeat this process thousands of times in order to ensure convergence and we also test our fits with several different random seeds, so as not to bias the results.

As soon as the GA has converged, the given best-fit function is an analytic and smooth function of the redshift  $z$  that describes the possible evolution of the coupling  $\zeta(z)$ .

The errors on this best-fit are estimated using an analytical approach developed by Nesseris & Garcia-Bellido (2012, 2013a), in which the errors are estimated by a path integral over the whole functional space. This approach has been exhaustively tested by Nesseris & Garcia-Bellido (2012) and has been found to be in very good agreement with Monte Carlo based error estimates.

The fact that in this approach we allow for a redshift dependence of the coupling  $\zeta$  allows us to examine whether our assumptions, which rely on a constant coupling, are still valid or they break down. This is done with the goal of obtaining a null test for the constancy of  $\zeta$  and the linear expansion of the gauge kinetic function in Sect. 2. Indeed, should a variation in  $\alpha$  be supported by the data, but generated by a mechanism that violates our assumptions, Eqs. (6) and (7) would not be able to model its redshift trend, and our reconstruction would yield a non-constant coupling  $\zeta(z)$ . Any statistically significant deviations from a constant value at any redshift will imply that our original hypothesis of a constant coupling may be violated. This is analogous (though not identical) to the reconstruction of a parameter quantifying possible distance duality violations, discussed in Martinelli et al. (2020). Effectively, our approach allows us to determine whether or not the data is consistent with a null value of the coupling, and how well this is constrained at various redshifts. This is also akin to constraining the behaviour of the coupling in different redshift bins.

In this work, the specific numerical implementation of the GA is based on the publicly available code Genetic Algorithms<sup>2</sup>. For more details and how they apply to the analysis of *Euclid* data, see also Martinelli et al. (2020).

## 6. Likelihood approach results

In this Section, we show the results of the analysis presented in Sect. 4. We recall that our goal is to illustrate how the use of

<sup>2</sup> <https://github.com/snesseris/Genetic-Algorithms>

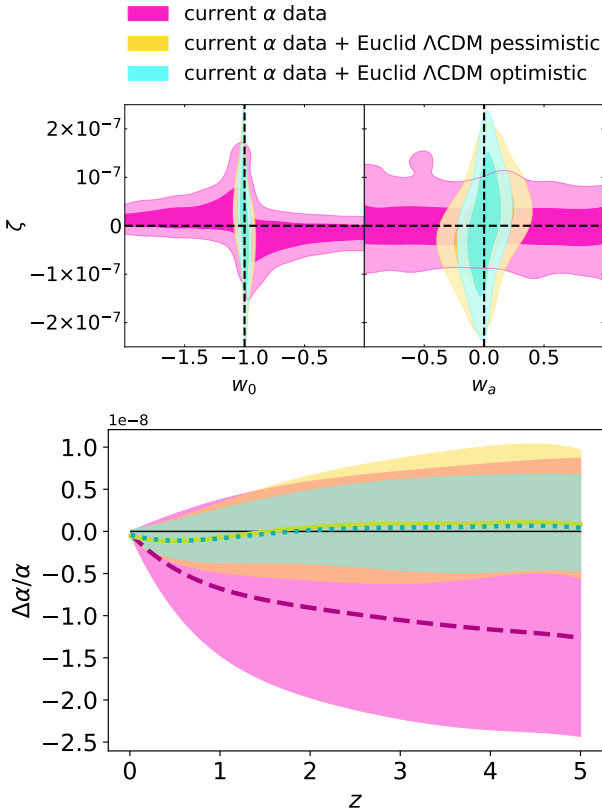


**Fig. 2.** *Top panel:* constraints on the CPL and coupling parameters using currently available data for  $\alpha$  measurements alone (purple contours) and in combination with *Euclid* forecast constraints with a  $\Lambda$ CDM fiducial (yellow contours for the pessimistic case and cyan contours for the optimistic case). *Bottom panel:* reconstruction of the mean trend in redshift of  $\Delta\alpha/\alpha$  and of the allowed 68% confidence level area, obtained interpolating the marginalized means and errors of the derived parameters described in Sect. 4. The purple dashed line and purple area refer to  $\alpha$  measurements alone, the yellow solid line and yellow area include *Euclid* in the pessimistic case, while the dotted green line and green contours combine the optimistic case.

external data allows *Euclid* to constrain dynamical dark energy models including an electromagnetic sector coupling. Specifically, the external data constrain the coupling  $\zeta$ , to which *Euclid* itself is insensitive. We first discuss the result of combining *Euclid* with currently available  $\Delta\alpha/\alpha$  and other current data, and focus on the analogous results when *Euclid* data is combined with next generation high-resolution spectroscopy data, specifically that expected from the ELT. Finally, we show the results of a Bayesian evidence analysis that quantifies the possible significance of a detection of a varying fine-structure constant.

### 6.1. *Euclid* and current $\alpha$ measurements

Figure 2 shows in purple the model parameter constraints obtained using currently available  $\alpha$  measurements, comprising the combination of Webb archival data and the dedicated  $\alpha$  measurements, atomic clocks constraints and the MICROSCOPE bound. The top panel shows the constraints on the free CPL and coupling parameters, while the bottom one highlights the reconstruction of the redshift trend of  $\Delta\alpha/\alpha$ . We show the results without and with *Euclid* data, for a  $\Lambda$ CDM fiducial, and for the *Euclid* data we show in yellow the pessimistic case and in cyan the optimistic one.

**Table 3.** Mean values and 68% c.l. bounds obtained using current  $\alpha$  measurements and their combination with *Euclid* forecasts.

	$\Lambda$ CDM fiducial		
	Current $\alpha$	+ <i>Euclid</i> pess	+ <i>Euclid</i> opt
$\Omega_m$	–	$0.3200 \pm 0.0035$	$0.3199 \pm 0.0018$
$w_0$	$-0.99 \pm 0.48$	$-1.000 \pm 0.036$	$-1.001 \pm 0.023$
$w_a$	–	$0.00 \pm 0.15$	$0.002 \pm 0.087$
$H_0$	$<75.2$	$67.00 \pm 0.36$	$67.00 \pm 0.10$
$\zeta 10^8$	$0.1^{+3.5}_{-3.9}$	$-0.1 \pm 8.2$	$0.4 \pm 8.9$
	$\zeta_{w_0 w_a}$ CDM fiducial		
	Current $\alpha$	+ <i>Euclid</i> pess	+ <i>Euclid</i> opt
$\Omega_m$	–	$0.3194 \pm 0.0038$	$0.3197 \pm 0.0019$
$w_0$	$-0.99 \pm 0.48$	$-0.948^{+0.034}_{-0.041}$	$-0.944 \pm 0.024$
$w_a$	–	$0.13^{+0.15}_{-0.14}$	$0.112 \pm 0.085$
$H_0$	$<75.2$	$66.98 \pm 0.37$	$67.00 \pm 0.10$
$\zeta 10^8$	$0.1^{+3.5}_{-3.9}$	$-3.6 \pm 5.9$	$-3.8 \pm 4.9$

**Notes.** Notice that in this case, as current  $\alpha$  data are used, the modified  $\zeta$  fiducial value of  $\zeta_{w_0 w_a}$ CDM does not affect the results, given that the fiducial cosmology is used only for *Euclid* data, which are not sensitive to this parameter.

In Table 3, it is possible to notice how the constraint on the coupling  $\zeta$  becomes less stringent when *Euclid* is included, changing from  $\zeta = (0.1^{+3.5}_{-3.9}) \times 10^{-8}$  to  $\zeta = (-0.1 \pm 8.2) \times 10^{-8}$  in the pessimistic case, and  $\zeta = (0.4 \pm 8.9) \times 10^{-8}$  when the *Euclid* optimistic configuration is used. The reason for such loosening of the bound is due to the ability of *Euclid* to tightly constrain the CPL parameters around the  $\Lambda$ CDM limit ( $w_0, w_a$ ) =  $(-1, 0)$ ; due to the degeneracy with  $\zeta$  – see Eqs. (6) and (7) – this makes the  $\alpha$  data less sensitive to the coupling parameter, as now a wider range of values is able to fit the data. Such a result is compatible with what was found in Calabrese et al. (2014), where other datasets able to tightly constrain the CPL parameters were considered. In the bottom panel of Fig. 2, it can be seen however how the weaker constrain on  $\zeta$  does not lead to a larger spread of the allowed  $\Delta\alpha/\alpha$  reconstructions, which are instead tightly constrained around the no-variation limit by the inclusion of *Euclid* information, exactly because of the tight constraints on the CPL parameters.

The situation changes when the *Euclid* results obtained for the  $\zeta_{w_0 w_a}$ CDM fiducial cosmology are used. In Fig. 3 it is possible to notice how in this case the *Euclid* bound centred on a non- $\Lambda$ CDM value of the CPL parameters breaks the degeneracy between these and  $\zeta$ . Here the loosening of the constraint on the coupling parameter is reduced, with the bound changing from  $\zeta = (0.1^{+3.5}_{-3.9}) \times 10^{-8}$  to  $\zeta = (-3.6 \pm 5.9) \times 10^{-8}$  (pessimistic) and  $\zeta = (-3.8 \pm 4.9) \times 10^{-8}$  (optimistic), and the constraint on the redshift trend of  $\Delta\alpha/\alpha$  is tightened around a non-vanishing variation in the fine-structure constant. The different behaviour of the bounds on  $\zeta$  when *Euclid* is included in the analysis is due here to the fact that the LSS information constrain the  $w_0$  and  $w_a$  parameters away from the  $\Lambda$ CDM limit; this implies that the degeneracy shown in the previous case is broken, and the  $\alpha$  data do not have a larger range of allowed coupling value.

While one can see that the inclusion of *Euclid* data helps  $\alpha$  measurements constrain the variation in this fundamental parameter (since it provides information on the cosmological

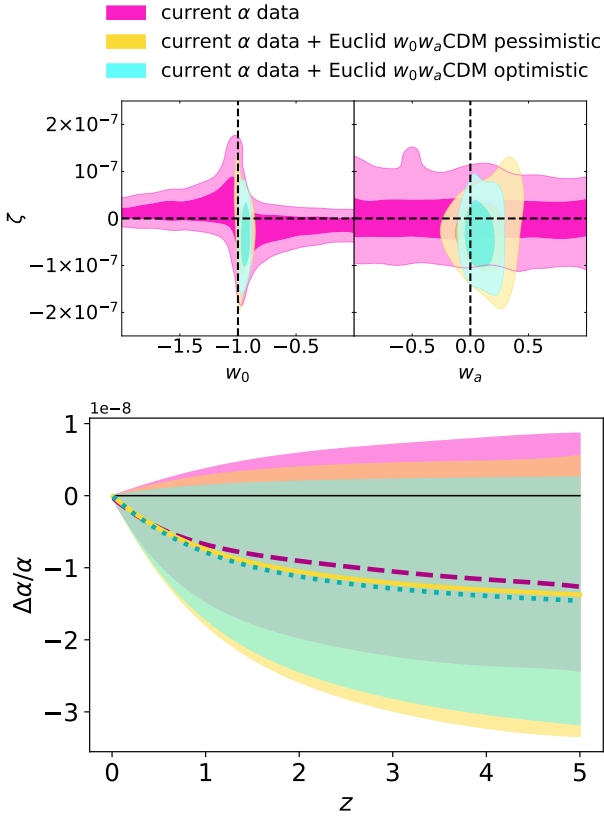


**Fig. 3.** Same as Fig. 2, but when the fiducial used to obtain the *Euclid* results is  $\zeta_{w_0w_a}\text{CDM}$ . Notice that here we use currently available direct measurements of  $\alpha$ , which are not impacted by our choice of fiducial cosmology. Thus, the modified  $\zeta$  fiducial value does not affect these results, as the *Euclid* probes considered are not sensitive to this parameter.

parameters), the synergy between these two datasets goes both ways: given the assumption done in Sect. 2 that the scalar field responsible for dark energy is the one that couples with the electromagnetic sector, the  $\alpha$  measurements also improve *Euclid* constraints on the CPL parameters, since *Euclid* on its own is not sensitive to  $\zeta$ . While this improvement is not extreme, it can be noticed in our results (see Table 3), where the errors on  $w_0$  and  $w_a$  are slightly improved with respect to the EC20 bounds shown in Sect. 3.3. The additional constraining power leads to an increase in the Figure of Merit (FoM), which we define as (EC20)

$$\text{FoM} = \sqrt{\det(C_{w_0, w_a})^{-1}}, \quad (19)$$

with  $C_{w_0, w_a}$  the covariance matrix, obtained from our MCMC results, marginalized over all parameters except for the CPL ones. In the  $\Lambda\text{CDM}$  fiducial, the combination of *Euclid* and  $\alpha$  data improves the FoM by 18% (13%) with respect to the *Euclid* pessimistic (optimistic) value alone. When instead the fiducial for  $w_0$  and  $w_a$  is shifted from the cosmological constant limit, such improvement becomes 3% in both the pessimistic and optimistic cases. Such a result comes from our assumption that the DE field is the one responsible for the variation in  $\alpha$ ; this relation makes the astrophysical data sensitive to the DE parameters  $w_0$  and  $w_a$ , while no contributions to the FoM would be added if the  $\alpha$  variation is not related to DE (or if one assumes a fixed vanishing coupling  $\zeta$ ).

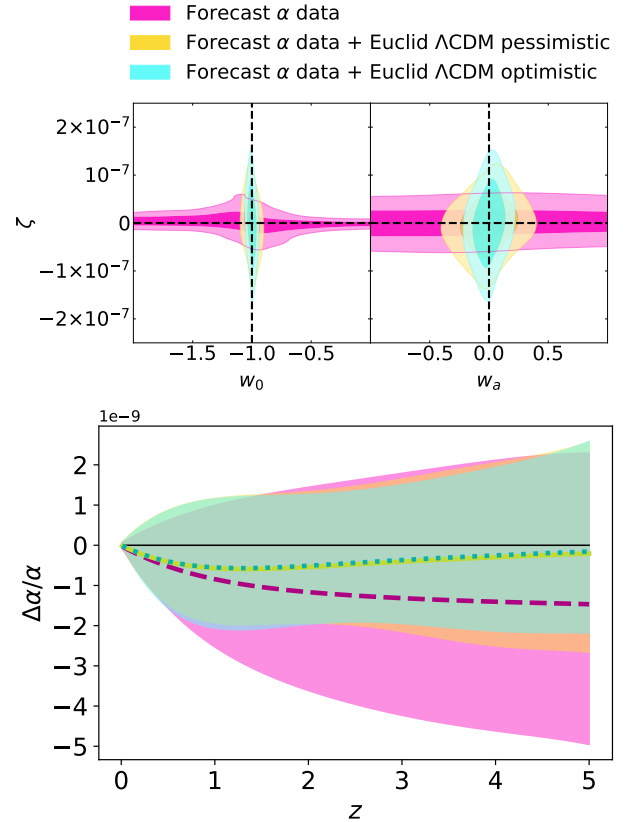


**Fig. 4.** Same as Fig. 2, but here the purple contours and lines refer to the forecast ELT data, while the yellow and cyan refer to the combination of this simulated dataset with pessimistic and optimistic *Euclid* results. The fiducial used here for both ELT and *Euclid* is the  $\Lambda\text{CDM}$  one shown in Table 1.

## 6.2. *Euclid* and the ELT

After quantifying the impact of current constraints on  $\alpha$  on *Euclid*, we now focus on the synergy between *Euclid* and the next generation high-resolution spectrograph for the ELT.

In Fig. 4 we show the results for the  $\Lambda\text{CDM}$  fiducial, with ELT constraints in purple, and those with the inclusion of pessimistic and optimistic *Euclid* data in yellow and cyan respectively. As for the current data case, we find that the inclusion of *Euclid* leads to a loosening of the constraints on the coupling parameter, see Table 4, but with a tightening of the reconstruction of  $\Delta\alpha/\alpha$  around the  $\Lambda\text{CDM}$  limit due to the information on  $w_0$  and  $w_a$  brought by *Euclid*.

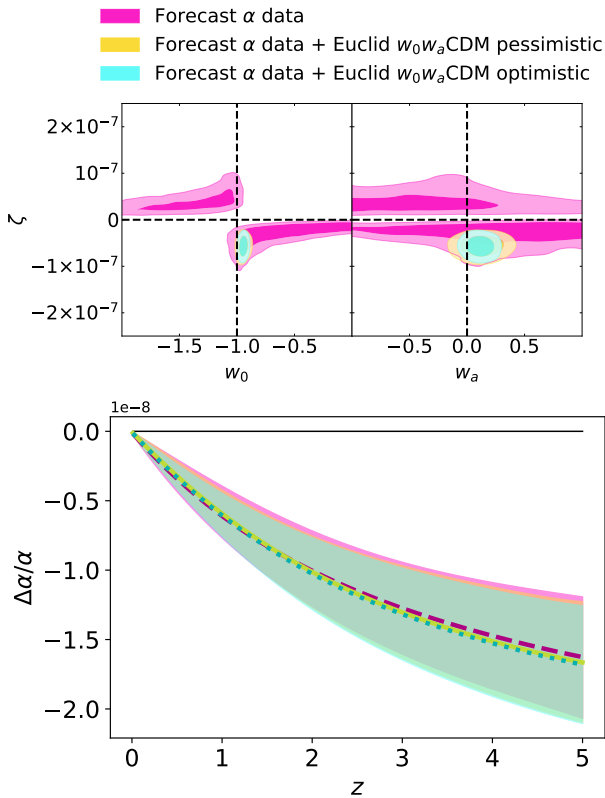
The results shown in Fig. 5 correspond to the  $\zeta_{w_0w_a}\text{CDM}$  fiducial of Table 1. The values chosen for this fiducial make the precise data of ELT incompatible with a vanishing  $\Delta\alpha/\alpha$  and this leads to a multimodal posterior distribution for the  $\zeta$ ,  $w_0$  and  $w_a$  parameters. Looking at Eqs. (6) and (7), the symmetry of these peaks with respect to the  $(\zeta, w_0, w_a) = (0, -1, 0)$  point in the parameter space appears evident, as simultaneously changing the sign of  $\zeta$  and  $1 + w(z)$  leads to the same low-redshift evolution of  $\Delta\alpha/\alpha$ . Because of this, when *Euclid* information is included, we find a breaking of the symmetry between the coupling and CPL parameters, with *Euclid* tightening the constraints on  $w_0$  and  $w_a$  around the fiducial.

Also in this case, as for current  $\alpha$  data, the inclusion of the information on  $\Delta\alpha/\alpha$  impacts the  $(w_0, w_a)$  FoM with respect to what is obtained with *Euclid* alone. In the  $\Lambda\text{CDM}$  fiducial, the FoM improves by 26% in both the pessimistic and optimistic



**Table 4.** Mean values and 68% c.l. bounds obtained using forecast  $\alpha$  data and their combination with *Euclid* forecasts.

	$\Lambda$ CDM fiducial		
	Forecast $\alpha$	+ <i>Euclid</i> pess	+ <i>Euclid</i> opt
$\Omega_m$	–	$0.3201 \pm 0.0037$	$0.3200 \pm 0.0018$
$w_0$	$-1.07 \pm 0.48$	$-0.9998 \pm 0.038$	$-1.000 \pm 0.023$
$w_a$	–	$0.00 \pm 0.15$	$0.000 \pm 0.085$
$H_0$	–	$67.00 \pm 0.33$	$67.000 \pm 0.093$
$\zeta 10^8$	$0.1 \pm 1.9$	$-0.1 \pm 4.8$	$-0.1 \pm 5.9$
	$\zeta w_0 w_a$ CDM fiducial		
	Forecast $\alpha$	+ <i>Euclid</i> pess	+ <i>Euclid</i> opt
$\Omega_m$	–	$0.3195 \pm 0.0034$	$0.3198 \pm 0.0019$
$w_0$	$-0.83^{+0.71}_{-0.30}$	$-0.946^{+0.029}_{-0.035}$	$-0.944 \pm 0.023$
$w_a$	–	$0.13 \pm 0.12$	$0.113 \pm 0.080$
$H_0$	$<76.1$	$66.96 \pm 0.36$	$66.993 \pm 0.099$
$\zeta 10^8$	$-0.5^{+4.3}_{-3.1}$	$-5.7^{+1.6}_{-1.4}$	$-5.7 \pm 1.5$


**Fig. 5.** Same as Fig. 4, but the fiducial cosmology used in this case is the  $\zeta w_0 w_a$ CDM of Table 1, thus a case that deviates from  $\Lambda$ CDM, with  $\zeta = -5 \times 10^{-8}$ ,  $w_0 = -0.94$ ,  $w_a = 0.1$ .

cases, while for the  $\zeta w_0 w_a$ CDM fiducial the improvement in the FoM becomes 8%.

### 6.3. Bayesian evidence

The results discussed in this Section make use of Metropolis-Hastings (MH) algorithm to sample the parameter space. This algorithm might fail in reconstructing the posterior shape when this is multimodal. Given the behaviour of some of our posterior distributions we compare the results obtained through MH

with those from a nested sampling approach, using the public polychord code (Handley et al. 2015a,b) available in Cobaya, finding compatible results.

Given our use of nested sampling, we obtain as a byproduct of our analysis pipeline an estimate of the Bayesian evidence for each of the cases considered. This allows us to perform a model selection analysis for the different fiducial and experimental settings being considered in this work. We take as reference the  $\Lambda$ CDM model, thus analyzing all the different data combinations fixing  $\zeta = 0$ ,  $w_0 = -1$ , and  $w_a = 0$ . Once the evidence  $Z_{\text{ref}}$  is computed for this model, we compare it with the evidence  $Z$  obtained when these parameters are free to vary. In all the cases considered, we assume the same priors on the cosmological parameters, and therefore their effect on the evidence calculation should cancel out. For the coupling  $\zeta$ , in the case in which this is free to vary, we always use the MICROSCOPE prior discussed in Sect. 3.1.

In Table 5 we show the difference of the logarithms of the evidence ( $K = \log Z - \log Z_{\text{ref}}$ ); here a positive value indicates a preference for the extended model, while a negative value supports the  $\Lambda$ CDM model. The results shown highlight how, assuming a  $\Lambda$ CDM fiducial, the model comparison favours the reference model (negative values) while for  $\zeta w_0 w_a$ CDM the extended model is supported. Thanks to the constraining power of *Euclid*, all the cases (pessimistic and optimistic) and for both current and forecast  $\alpha$  data provide “decisive” evidence for one or the other model according to the Jeffrey’s scale (Jeffreys 1939). However, it has been noted in Nesseris & Garcia-Bellido (2013b) that the values of the Jeffrey’s scale should be interpreted with caution, especially in cases of nested models, as they may lead to biased conclusions.

We note that the extreme values of  $K$  shown in Table 5 are mainly due to the constraining power of *Euclid* on  $w_0$  and  $w_a$ . If the reference model is taken to be a  $w_0 w_a$ CDM model, thus with  $\zeta = 0$ , but with  $w_0$  and  $w_a$  free to vary, the situation changes significantly. In the  $\Lambda$ CDM fiducial case, the comparison between a model with varying  $\alpha$  and the  $w_0 w_a$ CDM model is always inconclusive, as expected since both of them compare similarly with respect to the favoured  $\Lambda$ CDM model. If we move to the  $\zeta w_0 w_a$ CDM fiducial instead, when using current  $\alpha$  data, the comparison of the two models is still inconclusive, thus highlighting how the decisive preference with the previous reference was totally driven by *Euclid* constraints on CPL parameters, and that the sensitivity of current  $\alpha$  data do not allow to distinguish the model under examination here from a simple  $w_0 w_a$ CDM. The case of forecast data combined with *Euclid* instead still shows a decisive evidence in favour of the varying  $\alpha$  model, also with respect to the  $w_0 w_a$ CDM reference. This clearly shows how the improvement brought by the combination of ELT and *Euclid* is able to distinguish a varying  $\alpha$  model not only from the standard  $\Lambda$ CDM case, but also from a cosmology where the dark energy scalar field is not coupled to the electromagnetic sector.

## 7. Coupling null test results

In this Section we present the GA reconstruction of the coupling  $\zeta$  as a null test of whether any possible redshift dependence of  $\alpha$  could be detected through the combination of *Euclid* and current astrophysical data or future ELT data. We use a machine learning approach based on the GA to reconstruct  $\zeta$ , as this effectively provides a null test for the constancy of the gauge kinetic term and its linear expansion given by Eq. (2).

**Table 5.** Differences ( $K$ ) in the logarithm of the Bayesian evidence, between the extended model allowing for  $\alpha$  variation and the reference  $\Lambda$ CDM model.

	$\Lambda$ CDM fiducial			
	$\Lambda$ CDM reference	$w_0w_a$ CDM reference		
	Pessimistic	Optimistic	Pessimistic	Optimistic
Current $\alpha$	-5.8	-7.0	0.01	-0.27
Forecast $\alpha$	-6.4	-7.4	-0.65	-0.92
	$\zeta w_0w_a$ CDM fiducial			
	$\Lambda$ CDM reference	$w_0w_a$ CDM reference		
	Pessimistic	Optimistic	Pessimistic	Optimistic
Current $\alpha$	9.5	48.8	-0.32	-0.50
Forecast $\alpha$	15.6	55.1	5.96	5.71

**Notes.** The cases considered here only show the combination of *Euclid* and  $\alpha$  data.

### 7.1. *Euclid* and current $\alpha$ data results

First, we directly reconstruct the coupling  $\zeta$  using the currently available  $\alpha$  measurements, comprising the combination of Webb archival data and the dedicated  $\alpha$  measurements, atomic clocks constraints and the MICROSCOPE bound, together with the *Euclid* forecast constraints with a  $\zeta w_0w_a$ CDM fiducial. In the top panel of Fig. 6 we show the GA reconstruction of the coupling  $\zeta$  as a function of redshift (red line) together with the  $1\sigma$  error shaded region.

The nominal GA reconstruction of  $\zeta(z)$  is found to be

$$\zeta_{\text{GA}}(z) = -\frac{0.011 + z(1.558 + 3.041z)}{0.256 + z(1.011 + z)} \times 10^{-6}, \quad (20)$$

but as can be seen in the Figure,  $\zeta$  is fully consistent with zero within the errors. At high redshifts the GA leads to a value for the coupling of  $\zeta_{\text{GA}}(z \sim 4) \simeq (-2.704 \pm 8.293) \times 10^{-6}$ . On the other hand, at  $z = 0$  the GA gives the value  $\zeta_{\text{GA}}(z = 0) = (-4.285 \pm 1.510) \times 10^{-8}$ , which is in very good agreement with the parametric case when the coupling is assumed to be constant.

For completeness, in the bottom panel of Fig. 6 we show a reconstruction of the relative variation in the fine-structure constant  $\Delta\alpha/\alpha$  (red line), under the previously mentioned assumptions, in order to assess its redshift trend. Here the Webb archival data is shown in grey background points, while the dedicated  $\alpha$  measurements are shown in black background points. We confirm that the allowed  $\Delta\alpha/\alpha$  is tightly constrained around zero, even at high redshifts.

### 7.2. Synergy between *Euclid* and ELT

Next, we consider the scenario of combining *Euclid* data with the forecast ELT data, in the case where the fiducial model has a non-zero coupling. In the top panel of Fig. 7 we show the GA reconstruction of the coupling  $\zeta$  as a function of redshift (red line) using the forecast ELT  $\alpha$  measurements, together with the *Euclid* forecast constraints with a  $\zeta w_0w_a$ CDM fiducial. We use the same atomic clocks constraints and the MICROSCOPE as in the previous sub-section. We find that the GA reconstruction is consistent with the fiducial value (shown with the dot-dashed line) within the  $1\sigma$  bound. In particular, at high redshifts ( $z > 1$ ) a deviation from zero is detected, in agreement with the fiducial value used in our mocks, highlighting the importance of the extension of the redshift lever arm provided by the ELT measurements of  $\alpha$ .

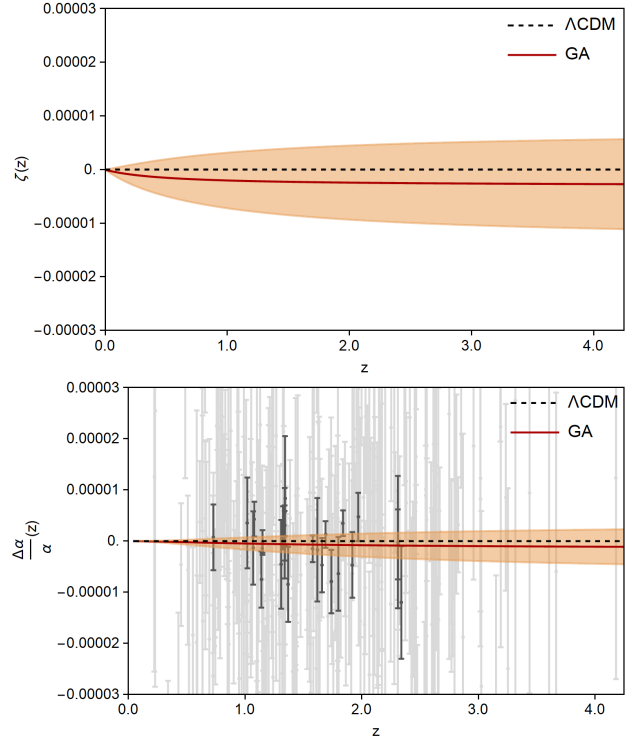


**Fig. 6.** *Top panel:* GA Reconstruction of the coupling  $\zeta$  as a function of redshift using the currently available  $\alpha$  measurements and *Euclid* forecast constraints with a  $\zeta w_0w_a$ CDM fiducial. *Bottom panel:* reconstruction of the relative variation in the fine-structure constant  $\Delta\alpha/\alpha$ . The Webb data is shown in grey background points and the dedicated  $\alpha$  measurements are shown in black background points. In both panels the red line corresponds to the GA reconstruction, while the shaded region is the  $1\sigma$  error.

In the bottom panel of Fig. 7 we also show a GA reconstruction of the relative variation in the fine-structure constant  $\Delta\alpha/\alpha$  (red line). As a test of our approach and given the much higher sensitivity of the ELT data, we also bin the data either in one bin (green point) or in two bins (blue points) splitting the ELT data at  $z = 2$ . We find that the GA reconstruction of the relative variation in the fine-structure constant is in excellent agreement with both the fiducial model, given by the dot-dashed line, and with the binning of the data.

## 8. Discussion and outlook

When studying theoretical models beyond the concordance  $\Lambda$ CDM framework, many realistic extensions introduce couplings between the different degrees of freedom. In particular, the coupling of physically realistic dynamical dark energy scalar fields to the electromagnetic sector will lead to a time dependence of the fine-structure constant (Carroll 1998; Dvali & Zaldarriaga 2002; Chiba & Kohri 2002), which could be detected and interpreted as a smoking gun for the existence of extra scalar fields. In this work we have studied the role of the forthcoming *Euclid* mission in constraining such theoretical models. *Euclid* will provide us with very precise cosmological information using the clustering of galaxies and the weak lensing measurements from the large-scale structure of the Universe. However, these probes are not enough to constrain the full parameter space of these models. We therefore need to add astrophysical (and local) data, specifically to constrain the coupling

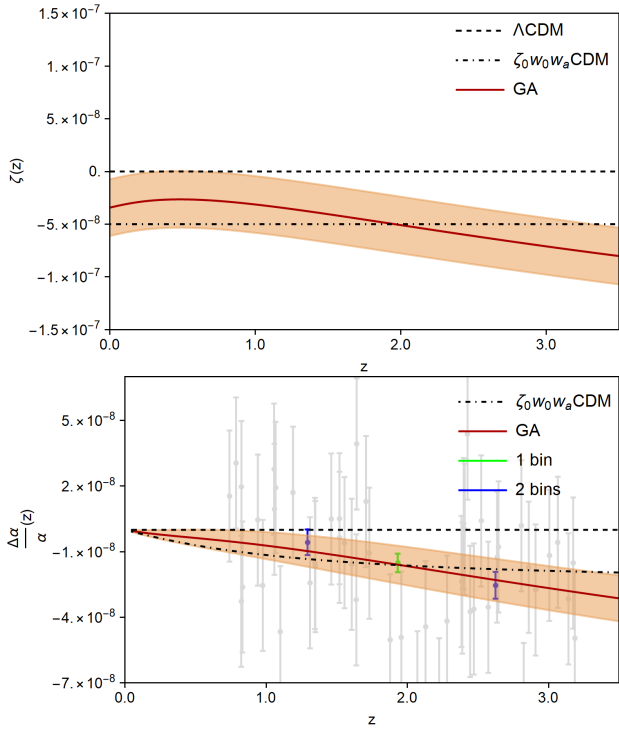


**Fig. 7.** *Top panel:* GA reconstruction of the coupling  $\zeta$  as a function of redshift (red line) using the forecast ELT  $\alpha$  data (grey background points), the atomic clocks constraints and the MICROSCOPE bound (both at  $z = 0$ ) and *Euclid* forecast constraints with a  $\zeta_{w_0 w_a}$ CDM fiducial. *Bottom panel:* reconstruction of the relative variation in the fine-structure constant  $\Delta\alpha/\alpha$  (red line) along with binned values of the data in one (green point) and two bins (blue points). In both cases the red line corresponds to the GA reconstruction, while the shaded region is the  $1\sigma$  error.

between the dark energy scalar field and the electromagnetic sector.

In this work we have considered current astrophysical tests of the stability of the fine-structure constant from quasi-stellar object spectral lines (both from archival data and from dedicated measurements), as well as current laboratory constraints on the present-day drift rate of  $\alpha$  from atomic clock experiments and constraints on the Eötvös parameter from the MICROSCOPE satellite. However, at the time *Euclid* data will be available we expect to have even more precise astrophysical measurements of  $\alpha$ , so we have also forecast the precision of the high-resolution ultra-stable spectrograph HIRES at the Extremely Large Telescope. We have used both a parametric approach, under a standard likelihood analysis, and a non-parametric machine learning class of stochastic optimization methods to forecast the constraints from the joint analysis of *Euclid* and astrophysical and local data.

Starting with the parametric approach, we have first considered the synergy between *Euclid* and current measurements of the relative variation in the fine-structure constant. Our baseline scenario has a  $\Lambda$ CDM fiducial, meaning that the fiducial corresponds to a vanishing coupling constant and a cosmological constant as dark energy. In Sect. 6.1 we have seen that *Euclid* very significantly restricts the allowed values of the fine-structure constant as a function of redshift compared to the constraints with astrophysical and laboratory data alone. This is due to *Euclid*'s ability to constrain the dark energy equation of state parameters. However, for this same reason, and because of the

degeneracy between the coupling constant and  $w_0$  and  $w_a$  when they are close to the cosmological constant corresponding values, the addition of *Euclid* data loosens the constraints on the coupling  $\zeta$  compared to the constraints from fine-structure constant data alone.

We have then performed the same analysis using the  $\zeta_{w_0 w_a}$ CDM fiducial for the *Euclid* results, where the coupling fiducial is non-null and the fiducial values of  $w_0$  and  $w_a$  no longer correspond to a cosmological constant. In this case the increase of constraining power on the evolution of  $\alpha$  when adding *Euclid* data is still present. Concerning the bounds on the coupling constant, the addition of *Euclid* data only marginally loosens the constraints, since the fiducial is not exactly on  $\Lambda$ CDM and the degeneracy between the coupling constant and the dark energy parameters is partially broken. It is also worth mentioning that adding these astrophysical and local tests of the variation in the fine-structure constant improves the constraints on the dark energy equation of state parameters from *Euclid* data alone, with the FoM for dark energy parameters improving between 3% and 18%, as long as the model considered connects the variation in  $\alpha$  to the dark energy parameters, thus making the  $\alpha$  data sensitive to them.

Still with the parametric approach, we have considered the synergy between *Euclid* and the ELT. The results obtained have been qualitatively the same, with *Euclid* data helping to constrain the evolution of the fine-structure constant as a function of redshift while the astrophysical and local data help constraining the dark energy equation of state. However, given the fact that the ELT data is much more precise than current measurements, the contribution of *Euclid* on  $\Delta\alpha/\alpha$  is proportionally somewhat smaller, while the contribution of ELT on  $w_0$  and  $w_a$  is slightly larger, with the FoM now improving between 8% and 26%. Furthermore, we also performed a model comparison analysis, which highlighted how both current and forecast  $\alpha$  data, in combination with *Euclid*, can significantly distinguish between  $\Lambda$ CDM and a model with a coupled scalar field, while only when considering ELT forecast can the latter be distinguished from a  $w_0 w_a$ CDM cosmology with a vanishing  $\zeta$  coupling.

We have also used a model-independent approach to reconstruct the coupling between the dark energy scalar field and the electromagnetic sector. This is effectively a null test reconstruction of the behaviour of the coupling  $\zeta$ . Specifically, any deviation from a constant coupling would either suggest unidentified systematics in the astrophysical data or indicate that the assumptions made in Sect. 2 break down and our modelling is not accurate enough to explain the observations; in the latter case this would imply that the putative dynamical dark energy and varying  $\alpha$  would not be due to the same underlying physical mechanism – which would in itself be a significant result. Our analysis shows how the GA are able to reconstruct the coupling function in agreement with the fiducial values assumed, and are compatible with a constant coupling.

Overall, we have found that the synergies between the main probes of *Euclid* and astrophysical measurements of  $\alpha$  can tightly constrain models where the dark energy scalar field is coupled to the electromagnetic sector. Moreover, recent analyses have shown that combining *Euclid* with future cosmic microwave background experiments will provide very precise constraints on the cosmological parameters (Euclid Collaboration 2021). Therefore, although the cosmic microwave background sensitivity to the fine-structure constant is not at the same level as astrophysical constraints, we can expect the improvement on cosmological parameter constraints to also propagate to the varying fine-structure constant model

considered in this work. In addition to these combinations of *Euclid* with external data, one must notice that other *Euclid* probes (such as a possible SNIa survey) can also be directly sensitive to a varying fine-structure constant, and this would further improve the contribution of *Euclid* on tests of such coupled models.

**Acknowledgements.** MM has received the support of a fellowship from “la Caixa” Foundation (ID 100010434), with fellowship code LCF/BQ/PI19/11690015, and the support of the Centro de Excelencia Severo Ochoa Program SEV-2016-059. The work of CJM was financed by FEDER – Fondo Europeo de Desarrollo Regional funds through the COMPETE 2020 – Operational Programme for Competitiveness and Internationalisation (POCI), and by Portuguese funds through FCT – Fundação para a Ciência e a Tecnologia in the framework of the project POCI-01-0145-FEDER-028987. IT acknowledges support from the Spanish Ministry of Science, Innovation and Universities through grant ESP2017-89838, and the H2020 programme of the European Commission through grant 776247. SN acknowledges support from the research project PGC2018-094773-B-C32, the Centro de Excelencia Severo Ochoa Program SEV-2016-059 and the Ramón y Cajal program through Grant No. RYC-2014-15843. The Euclid Consortium acknowledges the European Space Agency and a number of agencies and institutes that have supported the development of *Euclid*, in particular the Academy of Finland, the Agenzia Spaziale Italiana, the Belgian Science Policy, the Canadian Euclid Consortium, the Centre National d’Etudes Spatiales, the Deutsches Zentrum für Luft- und Raumfahrt, the Danish Space Research Institute, the Fundação para a Ciência e a Tecnologia, the Ministerio de Economía y Competitividad, the National Aeronautics and Space Administration, the Nederlandse Onderzoekschool Voor Astronomie, the Norwegian Space Agency, the Romanian Space Agency, the State Secretariat for Education, Research and Innovation (SERI) at the Swiss Space Office (SSO), and the United Kingdom Space Agency. A complete and detailed list is available on the *Euclid* web site (<http://www.euclid-ec.org>).

## References

- Akrami, Y., Scott, P., Edsjo, J., Conrad, J., & Bergstrom, L. 2010, *JHEP*, **04**, 057  
 Albareti, F. D., Comparat, J., Gutiérrez, C. M., et al. 2015, *MNRAS*, **452**, 4153  
 Arjona, R. 2020, *JCAP*, **08**, 009  
 Arjona, R., & Nesseris, S. 2020a, *PRD*, **101**, 123525  
 Arjona, R., & Nesseris, S. 2020b, *JCAP*, **11**, 042  
 Astier, P., Balland, C., Brescia, M., et al. 2014, *A&A*, **572**, A80  
 Bogdanos, C., & Nesseris, S. 2009, *JCAP*, **05**, 006  
 Calabrese, E., Menegoni, E., Martins, C. J. A. P., Melchiorri, A., & Rocha, G. 2011, *PRD*, **84**, 023518  
 Calabrese, E., Martinelli, M., Pandolfi, S., et al. 2014, *PRD*, **89**, 083509  
 Carroll, S. M. 1998, *PRL*, **81**, 3067  
 Casas, J. A., Garcia-Bellido, J., & Quiros, M. 1991, *Nucl. Phys. B*, **361**, 713  
 Casas, J. A., Garcia-Bellido, J., & Quiros, M. 1992, *Class. Quant. Grav.*, **9**, 1371  
 Cattoen, C., & Visser, M. 2007, ArXiv e-prints [arXiv:gr-qc/0703122]  
 Chevallier, M., & Polarski, D. 2001, *Int. J. Mod. Phys. D*, **10**, 213  
 Chiba, T., & Kohri, K. 2002, *Prog. Theor. Phys.*, **107**, 631  
 Costille, A., Caillat, A., Rossin, C., et al. 2018, in *Space Telescopes and Instrumentation 2018: Optical, Infrared, and Millimeter Wave*, eds. M. Lystrup, G. G. Fazio, et al., *SPIE*, **10698**, 730  
 Cropper, M., Pottinger, S., Azzollini, R., et al. 2018, in *Space Telescopes and Instrumentation 2018: Optical, Infrared, and Millimeter Wave*, eds. M. Lystrup, H. A. MacEwen, G. G. Fazio, et al., *SPIE*, **10698**, 709  
 Damour, T., & Donoghue, J. F. 2010, *Class. Quant. Grav.*, **27**, 202001  
 Damour, T., Piazza, F., & Veneziano, G. 2002, *Phys. Rev. Lett.*, **89**, 081601  
 Davis, E. D., & Hamdan, L. 2015, *Phys. Rev. C*, **92**, 014319  
 Deshpande, A. C., Kitching, T. D., Cardone, V. F., et al. 2020, *A&A*, **636**, A95  
 Dicke, R. H. 1964, *Relativité, Groupes et Topologie: Proceedings, École d’été de Physique Théorique, Session XIII, Les Houches*, 165  
 Dvali, G., & Zaldarriaga, M. 2002, *PRL*, **88**, 091303  
 Euclid Collaboration (Blanchard, A., et al.) 2020, *A&A*, **642**, A191  
 Euclid Collaboration (Ilić, S., et al.) 2021, *A&A*, in press, <https://doi.org/10.1051/0004-6361/202141556>  
 Fang, W., Hu, W., & Lewis, A. 2008, *PRD*, **78**, 087303  
 Fujii, Y., Iwamoto, A., Fukahori, T., et al. 2002, *J. Nucl. Sci. Tech.*, **39**, 592  
 Guimaraes, A. C., & Lima, J. A. S. 2011, *Class. Quant. Grav.*, **28**, 125026  
 Handley, W. J., Hobson, M. P., & Lasenby, A. N. 2015a, *MNRAS*, **450**, L61  
 Handley, W. J., Hobson, M. P., & Lasenby, A. N. 2015b, *MNRAS*, **453**, 4385  
 Hu, W. 2008, *PRD*, **77**, 103524  
 Hu, W., & Sawicki, I. 2007, *PRD*, **76**, 104043  
 Jeffreys, H. 1939, *The Theory of Probability*, Oxford Classic Texts in the Physical Sciences  
 Kilbinger, M., Heymans, C., Asgari, M., et al. 2017, *MNRAS*, **472**, 2126  
 Kitching, T. D., Alsing, J., Heavens, A. F., et al. 2017, *MNRAS*, **469**, 2737  
 Lange, R., Huntemann, N., Rahm, J., et al. 2021, *PRL*, **126**, 011102  
 Laureijs, R., Amiaux, J., Arduini, S., et al. 2011, ArXiv e-prints [arXiv:1110.3193]  
 Lazkoz, R., Alcaniz, J., Escamilla-Rivera, C., Salzano, V., & Sendra, I. 2013, *JCAP*, **12**, 005  
 Leite, A., Martins, C., Molaro, P., Corre, D., & Cristiani, S. 2016, *PRD*, **94**, 123512  
 Lewis, A. 2013, *PRD*, **87**, 103529  
 Lewis, A., & Bridle, S. 2002, *PRD*, **66**, 103511  
 Linder, E. V. 2003, *PRL*, **90**, 091301  
 Liske, J., Bono, G., Cepa, J., et al. 2014, *Top Level Requirements For ELT-HIRES*, Tech. rep., Document ESO 204697 Version 1  
 Marconi, A., Abreu, M., Adibekyan, V., et al. 2020, *SPIE Conf. Ser.*, **11447**, 1144726  
 Martinelli, M., Martins, C. J. A. P., Nesseris, S., et al. 2020, *A&A*, **644**, A80  
 Martins, C., Pinho, A., Carreira, P., et al. 2016, *PRD*, **93**, 023506  
 Martins, C. J. A. P. 2017, *Rep. Prog. Phys.*, **80**, 126902  
 Martins, C. J. A. P., & Vila Miñana, M. 2019, *Phys. Dark Univ.*, **25**, 100301  
 Milaković, D., Lee, C.-C., Carswell, R. F., et al. 2021, *MNRAS*, **500**, 1  
 Murphy, M. T., & Cooksey, K. L. 2017, *MNRAS*, **471**, 4930  
 Nesseris, S., & Garcia-Bellido, J. 2012, *JCAP*, **11**, 033  
 Nesseris, S., & Garcia-Bellido, J. 2013a, *PRD*, **88**, 063521  
 Nesseris, S., & Garcia-Bellido, J. 2013b, *JCAP*, **08**, 036  
 Nesseris, S., & Shafieloo, A. 2010, *MNRAS*, **408**, 1879  
 Nunes, N. J., & Lidsey, J. E. 2004, *PRD*, **69**, 123511  
 Olive, K. A., & Pospelov, M. 2008, *Phys. Rev. D*, **77**, 043524  
 Olive, K. A., Pospelov, M., Qian, Y.-Z., et al. 2004, *Phys. Rev. D*, **69**, 027701  
 Pinho, A. M. M., Martinelli, M., & Martins, C. J. A. P. 2017, *Phys. Lett. B*, **769**, 491  
 Planck Collaboration VI. 2020, *A&A*, **641**, A6  
 Sapone, D., Majerotto, E., & Nesseris, S. 2014, *PRD*, **90**, 023012  
 Silva, M. F., Winther, H. A., Mota, D. F., & Martins, C. J. A. P. 2014, *PRD*, **89**, 024025  
 Taylor, P. L., Kitching, T. D., McEwen, J. D., & Tram, T. 2018, *PRD*, **98**, 023522  
 Taylor, T. R., & Veneziano, G. 1988, *Phys. Lett. B*, **213**, 450  
 Torrado, J., & Lewis, A. 2021, *JCAP*, **05**, 057  
 Touboul, P., Métris, G., Rodrigues, M., et al. 2019, *Class. Quant. Grav.*, **36**, 225006  
 Tutusaus, I., Martinelli, M., Cardone, V. F., et al. 2020, *A&A*, **643**, A70  
 Vielzeuf, P. E., & Martins, C. J. A. P. 2014, *Mem. Soc. Ast. It.*, **85**, 155  
 Webb, J., King, J., Murphy, M., et al. 2011, *PRL*, **107**, 191101  
 Welsh, L., Cooke, R., Fumagalli, M., & Pettini, M. 2020, *MNRAS*, **494**, 1411  
 Whitmore, J. B., & Murphy, M. T. 2015, *MNRAS*, **447**, 446  
 Yahia-Cherif, S., Blanchard, A., Camera, S., et al. 2021, *A&A*, **649**, A52

<sup>1</sup> Instituto de Física Teórica UAM-CSIC, Campus de Cantoblanco, 28049 Madrid, Spain

e-mail: [matteo.martinelli@uam.es](mailto:matteo.martinelli@uam.es)

<sup>2</sup> Centro de Astrofísica da Universidade do Porto, Rua das Estrelas, 4150-762 Porto, Portugal

<sup>3</sup> Instituto de Astrofísica e Ciências do Espaço, Universidade do Porto, CAUP, Rua das Estrelas, 4150-762 Porto, Portugal

<sup>4</sup> Institute of Space Sciences (ICE, CSIC), Campus UAB, Carrer de Can Magrans, s/n, 08193 Barcelona, Spain

<sup>5</sup> Institut de Recherche en Astrophysique et Planétologie (IRAP), Université de Toulouse, CNRS, UPS, CNES, 14 Av. Edouard Belin, 31400 Toulouse, France

<sup>6</sup> Institut d’Estudis Espacials de Catalunya (IEEC), Carrer Gran Capità 2-4, 08034 Barcelona, Spain

<sup>7</sup> INFN-Sezione di Torino, Via P. Giuria 1, 10125 Torino, Italy

<sup>8</sup> Dipartimento di Fisica, Università degli Studi di Torino, Via P. Giuria 1, 10125 Torino, Italy

<sup>9</sup> INAF-Osservatorio Astrofisico di Torino, Via Osservatorio 20, 10025 Pino Torinese, TO, Italy

<sup>10</sup> INAF-IASF Milano, Via Alfonso Corti 12, 20133 Milano, Italy

<sup>11</sup> AIM, CEA, CNRS, Université Paris-Saclay, Université de Paris, 91191 Gif-sur-Yvette, France

<sup>12</sup> Université St Joseph; UR EGFEM, Faculty of Sciences, Beirut, Lebanon

<sup>13</sup> Astrophysics Research Institute, Liverpool John Moores University, 146 Brownlow Hill, Liverpool L3 5RF, UK

- <sup>14</sup> Departamento de Física, FCFM, Universidad de Chile, Blanco Encalada 2008, Santiago, Chile
- <sup>15</sup> Institute of Cosmology and Gravitation, University of Portsmouth, Portsmouth PO1 3FX, UK
- <sup>16</sup> INAF-Osservatorio di Astrofisica e Scienza dello Spazio di Bologna, Via Piero Gobetti 93/3, 40129 Bologna, Italy
- <sup>17</sup> Max Planck Institute for Extraterrestrial Physics, Giessenbachstr. 1, 85748 Garching, Germany
- <sup>18</sup> INFN-Sezione di Roma Tre, Via della Vasca Navale 84, 00146 Roma, Italy
- <sup>19</sup> Department of Mathematics and Physics, Roma Tre University, Via della Vasca Navale 84, 00146 Rome, Italy
- <sup>20</sup> Institut de Física d'Altes Energies (IFAE), The Barcelona Institute of Science and Technology, Campus UAB, 08193 Bellaterra, Barcelona, Spain
- <sup>21</sup> INAF-Osservatorio Astronomico di Roma, Via Frascati 33, 00078 Monteporzio Catone, Italy
- <sup>22</sup> Department of Physics "E. Pancini", University Federico II, Via Cinthia 6, 80126 Napoli, Italy
- <sup>23</sup> INFN section of Naples, Via Cinthia 6, 80126 Napoli, Italy
- <sup>24</sup> INAF-Osservatorio Astronomico di Capodimonte, Via Moiriello 16, 80131 Napoli, Italy
- <sup>25</sup> Dipartimento di Fisica e Astronomia 'Augusto Righi' – Alma Mater Studiorum Università di Bologna, Via Piero Gobetti 93/2, 40129 Bologna, Italy
- <sup>26</sup> INFN-Osservatorio Astrofisico di Arcetri, Largo E. Fermi 5, 50125 Firenze, Italy
- <sup>27</sup> Institut national de physique nucléaire et de physique des particules, 3 rue Michel-Ange, 75794 Paris Cédex 16, France
- <sup>28</sup> Centre National d'Etudes Spatiales, Toulouse, France
- <sup>29</sup> Aix-Marseille Univ, CNRS, CNES, LAM, Marseille, France
- <sup>30</sup> Department of Astronomy, University of Geneva, ch. d'Écogia 16 1290 Versoix, Switzerland
- <sup>31</sup> Université Paris-Saclay, CNRS, Institut d'astrophysique spatiale, 91405 Orsay, France
- <sup>32</sup> INFN-Padova, Via Marzolo 8, 35131 Padova, Italy
- <sup>33</sup> Univ. Lyon, Univ. Claude Bernard Lyon 1, CNRS/IN2P3, IP2I Lyon, UMR 5822, 69622 Villeurbanne, France
- <sup>34</sup> INAF-Osservatorio Astronomico di Trieste, Via G. B. Tiepolo 11, 34131 Trieste, Italy
- <sup>35</sup> Istituto Nazionale di Astrofisica (INAF) – Osservatorio di Astrofisica e Scienza dello Spazio (OAS), Via Gobetti 93/3, 40127 Bologna, Italy
- <sup>36</sup> Istituto Nazionale di Fisica Nucleare, Sezione di Bologna, Via Irnerio 46, 40126 Bologna, Italy
- <sup>37</sup> INAF-Osservatorio Astronomico di Padova, Via dell'Osservatorio 5, 35122 Padova, Italy
- <sup>38</sup> Universitäts-Sternwarte München, Fakultät für Physik, Ludwig-Maximilians-Universität München, Scheinerstrasse 1, 81679 München, Germany
- <sup>39</sup> Institute of Theoretical Astrophysics, University of Oslo, PO Box 1029, Blindern 0315, Oslo, Norway
- <sup>40</sup> Jet Propulsion Laboratory, California Institute of Technology, 4800 Oak Grove Drive, Pasadena, CA 91109, USA
- <sup>41</sup> von Hoerner and Sulger GmbH, Schloßplatz 8, 68723 Schwetzingen, Germany
- <sup>42</sup> Max-Planck-Institut für Astronomie, Königstuhl 17, 69117 Heidelberg, Germany
- <sup>43</sup> Université de Genève, Département de Physique Théorique and Centre for Astroparticle Physics, 24 quai Ernest-Ansermet, 1211 Genève 4, Switzerland
- <sup>44</sup> Department of Physics and Helsinki Institute of Physics, Gustaf Hällströmin katu 2, 00014 University of Helsinki, Finland
- <sup>45</sup> NOVA optical infrared instrumentation group at ASTRON, Oude Hoogeveensedijk 4, 7991 PD Dwingeloo, The Netherlands
- <sup>46</sup> Argelander-Institut für Astronomie, Universität Bonn, Auf dem Hügel 71, 53121 Bonn, Germany
- <sup>47</sup> Institute for Computational Cosmology, Department of Physics, Durham University, South Road, Durham DH1 3LE, UK
- <sup>48</sup> INFN-Bologna, Via Irnerio 46, 40126 Bologna, Italy
- <sup>49</sup> Observatoire de Sauverny, Ecole Polytechnique Fédérale de Lausanne, 1290 Versoix, Switzerland
- <sup>50</sup> INFN-Sezione di Bologna, Viale Berti Pichat 6/2, 40127 Bologna, Italy
- <sup>51</sup> European Space Agency/ESTEC, Keplerlaan 1, 2201 AZ Noordwijk, The Netherlands
- <sup>52</sup> Department of Physics and Astronomy, University of Aarhus, Ny Munkegade 120, 8000 Aarhus C, Denmark
- <sup>53</sup> Institute of Space Science, Bucharest 077125, Romania
- <sup>54</sup> Departamento de Astrofísica, Universidad de La Laguna, 38206 La Laguna, Tenerife, Spain
- <sup>55</sup> Instituto de Astrofísica de Canarias, Calle Vía Láctea s/n, 38204 San Cristóbal de la Laguna, Tenerife, Spain
- <sup>56</sup> Aix-Marseille Univ, CNRS/IN2P3, CPPM, Marseille, France
- <sup>57</sup> Dipartimento di Fisica e Astronomia "G. Galilei", Università di Padova, Via Marzolo 8, 35131 Padova, Italy
- <sup>58</sup> Institute for Astronomy, University of Edinburgh, Royal Observatory, Blackford Hill, Edinburgh EH9 3HJ, UK
- <sup>59</sup> Instituto de Astrofísica e Ciências do Espaço, Faculdade de Ciências, Universidade de Lisboa, Tapada da Ajuda, 1349-018 Lisboa, Portugal
- <sup>60</sup> Departamento de Física, Faculdade de Ciências, Universidade de Lisboa, Edifício C8, Campo Grande, 1749-016 Lisboa, Portugal
- <sup>61</sup> Universidad Politécnica de Cartagena, Departamento de Electrónica y Tecnología de Computadoras, 30202 Cartagena, Spain
- <sup>62</sup> Infrared Processing and Analysis Center, California Institute of Technology, Pasadena, CA 91125, USA
- <sup>63</sup> Dipartimento di Fisica e Astronomia, Università di Bologna, Via Gobetti 93/2, 40129 Bologna Italy
- <sup>64</sup> European Space Agency/ESRIN, Largo Galileo Galilei 1, 00044 Frascati, Roma, Italy
- <sup>65</sup> ESAC/ESA, Camino Bajo del Castillo, s/n., Urb. Villafranca del Castillo, 28692 Villanueva de la Cañada, Madrid, Spain
- <sup>66</sup> School of Physics and Astronomy, Cardiff University, The Parade, Cardiff CF24 3AA, UK
- <sup>67</sup> INAF-IASF Bologna, Via Piero Gobetti 101, 40129 Bologna, Italy
- <sup>68</sup> APC, AstroParticule et Cosmologie, Université Paris Diderot, CNRS/IN2P3, CEA/Irfu, Observatoire de Paris, Sorbonne Paris Cité, 10 rue Alice Domon et Léonie Duquet, 75205 Paris Cedex 13, France
- <sup>69</sup> Space Science Data Center, Italian Space Agency, Via del Politecnico snc, 00133 Roma, Italy

## Appendix A: Current data compatibility

As pointed out in Martins (2017), Martins & Vila Miñana (2019), the currently available astrophysical tests of the stability of the fine-structure constant are in slight tension with each other; the weighted mean of  $\Delta\alpha/\alpha$  obtained through the Webb archival data is in fact in tension of  $\approx 2\sigma$  with the one obtained through the recent dedicated measurements. In order to be able to combine these datasets, as we did throughout our paper, we must assess the significance of such tension.

In the parametric approach, we can estimate the concordance of the datasets by computing the Bayesian ratio

$$K = \frac{Z(\text{Webb} + \text{recent})}{Z(\text{Webb})Z(\text{recent})}, \quad (\text{A.1})$$

where  $Z(\text{Webb})$  is the evidence when using Webb data alone,  $Z(\text{recent})$  when only recent data are considered and  $Z(\text{Webb} + \text{recent})$  the case when the two are considered in combination. Such a Bayesian ratio can be used for model comparison between the case in which the two datasets are used to fit the same set of cosmological parameter,  $Z(\text{Webb} + \text{recent})$ , and the case in which these might differ for the two datasets,  $Z(\text{Webb})Z(\text{recent})$ .

We obtain these values using `polychord` to sample our free parameters and, when considering only astrophysical  $\alpha$  measurements, we find that  $\ln K \approx 0.2$ , a value that is not able to provide any conclusive evidence for either the concordance or discordance of the data. When instead we include the information brought by local measurements, we obtain  $\ln K \approx 1.6$ , thus an improved significance towards the concordance of the data. Such an increase in the value of  $\ln K$  comes from the fact that the local measurements dominate the constraints obtained through the parametric approach, thus hiding any possible discordance of the two sets of astrophysical data.

This does not apply in our null test reconstruction of  $\zeta(z)$ ; here, the local measurements only contribute to the very low redshift reconstruction, while astrophysical data dominate at higher redshift. Because of this tension between the Webb archival data and the recent dedicated measurement, the reconstruction performed with the GA attempts to be in agreement with both datasets, and this can potentially increase the error on the recon-

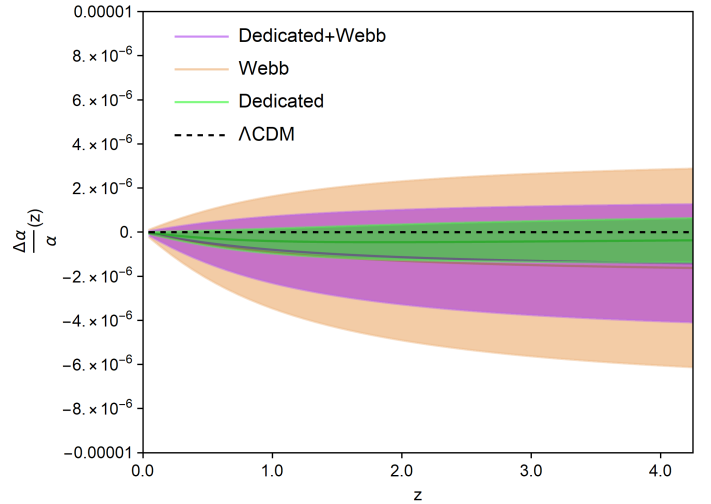


**Fig. A.1.** GA reconstruction of the relative variation in the fine-structure constant  $\Delta\alpha/\alpha$  as a function of redshift. The green line corresponds to the dedicated measurements, the orange line to the Webb archival data and the magenta line to the combination of the two, while in all cases the shaded region is the  $1\sigma$  error.

structed function. One thus expects that removing one of the datasets, the error on the reconstruction will decrease.

In particular, in Fig. A.1 we show the GA reconstruction of the relative variation in the fine-structure constant  $\Delta\alpha/\alpha$  as a function of redshift. The green line corresponds to the dedicated measurements, the orange line to the Webb archival data and the magenta line to the combination of the two, while in all cases the shaded region is the  $1\sigma$  error. As expected, the reconstruction of the dedicated measurements has a smaller error (green shaded region), but when we combine them with the Webb archival data then the combined error region not only does not decrease, but instead increases due to the tension, as observed in the magenta shaded region. Equivalently, we see that when we remove the Webb data from the combination of the two, counter-intuitively the error of the reconstruction decreases. However, overall the reconstructions are still compatible with each other and with zero.